

# Characterization of the sTGC Detectors and Reconstruction of Muons at ATLAS

Undergraduate Honours Thesis  
Final Report

PHYS 4909  
Winter 2025

**Renée de la Peña Lomeli**  
Student ID: 101224754

**Supervisor: Dr. Bellerive**

April 21, 2025

## Abstract

This project aimed to evaluate and optimize the muon tracking performance of the sTGC subsystem within the ATLAS New Small Wheel (NSW). Emphasis was placed on developing a reliable error estimator for strip hit spatial measurements, which are critical for accurate pattern recognition and track reconstruction. Both Monte Carlo simulations and real collision data were analyzed using ROOT and implemented to refine cluster characterization and enhance the spatial resolution of the strip readout system. The results showed that the Caruana method provided better spatial resolution and served as a more effective error estimator compared to the centroid method. As a next step, the parameterized error model will be integrated into future pattern recognition algorithms, with the goal of improving the intrinsic spatial resolution by approximately  $5\mu\text{m}$ .

# Contents

<b>1</b>	<b>Introduction</b>	<b>3</b>
<b>2</b>	<b>Apparatus</b>	<b>4</b>
2.1	sTGC Basics . . . . .	4
2.2	Strip Geometry and Readout . . . . .	6
<b>3</b>	<b>Theory</b>	<b>7</b>
<b>4</b>	<b>Measured Variables and Methodology</b>	<b>8</b>
4.1	Digitization . . . . .	9
4.1.1	Cluster Multiplicity . . . . .	9
4.1.2	Truth Residual . . . . .	10
4.2	Reconstruction . . . . .	11
4.2.1	Error Parametrization . . . . .	11
4.2.2	Track Residual . . . . .	13
4.2.3	Resolution . . . . .	14
4.2.4	Pull . . . . .	15
4.2.5	Efficiency . . . . .	17
<b>5</b>	<b>Development and Implementation</b>	<b>18</b>
5.1	1st Term . . . . .	18
5.2	2nd Term . . . . .	22
<b>6</b>	<b>Results</b>	<b>24</b>
<b>7</b>	<b>Conclusion</b>	<b>27</b>
	<b>References</b>	<b>28</b>

# 1 Introduction

The purpose of this project was to evaluate and optimize the muon tracking performance of the Small-strip Thin Gap Chambers (sTGC) subsystem within the ATLAS New Small Wheel (NSW) at CERN. Specifically, the work focused on developing a reliable error estimator for the strip hit spatial measurements used in advanced pattern recognition algorithms. These algorithms were applied to reconstruct muon tracks using both Monte Carlo simulations and real collision data. The parametrization developed in this project is intended for future implementation in pattern recognition, with the goal of improving strip spatial resolution by approximately  $5\mu\text{m}$ .

The NSW spectrometer upgrade completed in 2022, marked the largest detector upgrade in Phase I among the LHC experiments [1]. This upgrade is a pivotal component of the broader luminosity upgrade of the LHC. Motivated by the need to precisely study the Higgs sector, improve online muon identification capabilities and extend the sensitivity to new physics phenomena in the multi-TeV range [2]. This upgrade required the replacement of the existing ATLAS inner muon end-caps with the new set of NSW detectors. To accomplish the requirements for precise position resolution, efficiency, and timing at the anticipated high background rate, two technologies were implemented into the NSW subsystem. Namely, the Micro-Mesh Gaseous Structures (MicroMegas, MM) and small-strip Thin Gas Chamber (sTGC) were selected. The NSW configuration consists of sixteen detector planes organized into four multilayers, each containing four planes. The layers are arranged in sTGC-MM-MM-sTGC stacked manner in order to maximize the distance between the two sTGCs multilayers, as seen in Fig. 1. This sequence aids in improving the track segment angular resolution at the trigger level [2].

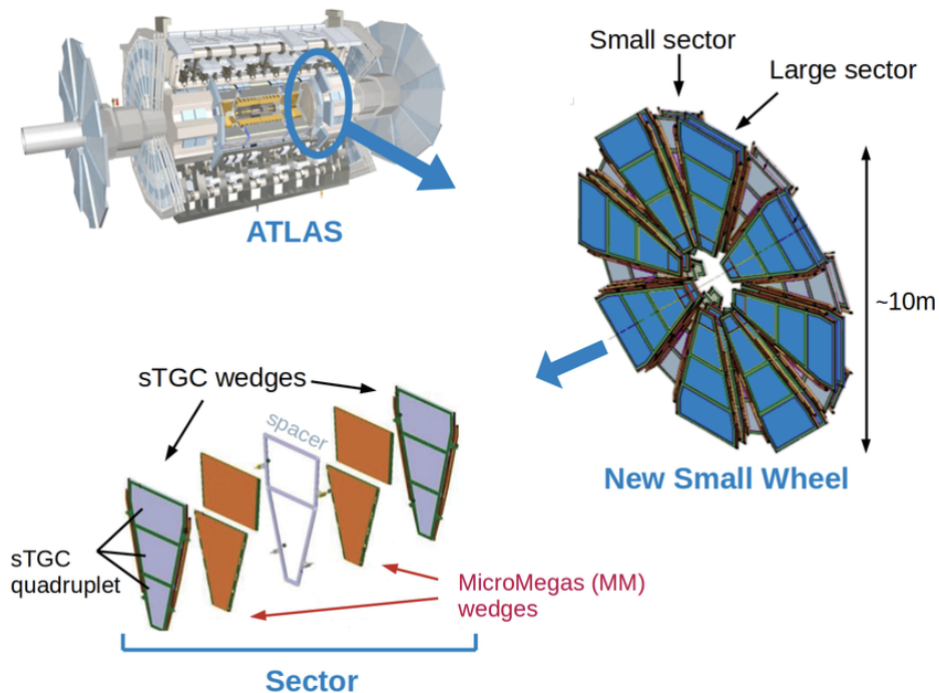


Figure 1: Schematic diagram of the sTGC's placement on the NSW and within the ATLAS detector [3]

The eight-plane configuration of each detector was designed to meet the requirements for a robust and fully operational system over its expected lifetime. Notably, the NSW upgrade represents the first large-scale deployment of micro-pattern gaseous detectors in a high-energy physics experiment. To support this system, a custom electronics architecture comprising approximately 2.5 million readout channels was developed, enabling both rapid triggering and precise muon tracking [4].

## 2 Apparatus

Real data were obtained from the sTGC subsystems in ATLAS, while simulated data were generated using corresponding detector parameters. This section outlines the fundamental aspects of the sTGC geometry, composition, and readout, with a specific focus on the strip component and its associated measurements.

### 2.1 sTGC Basics

The basic structure of the Small-strip Thin Gap Chambers (sTGC) consists of a grid of  $50\ \mu\text{m}$  gold plated tungsten wires held at 2.9 kV, with a pitch of 1.8 mm positioned between two cathode planes at a distance of 1.4 mm from the wire plane, as shown in Fig.2 [1]. Each sTGC quadruplet comprises four pad-wire-strip planes and functions as a Multiwire proportional chamber for precise muon detection and fast triggering.

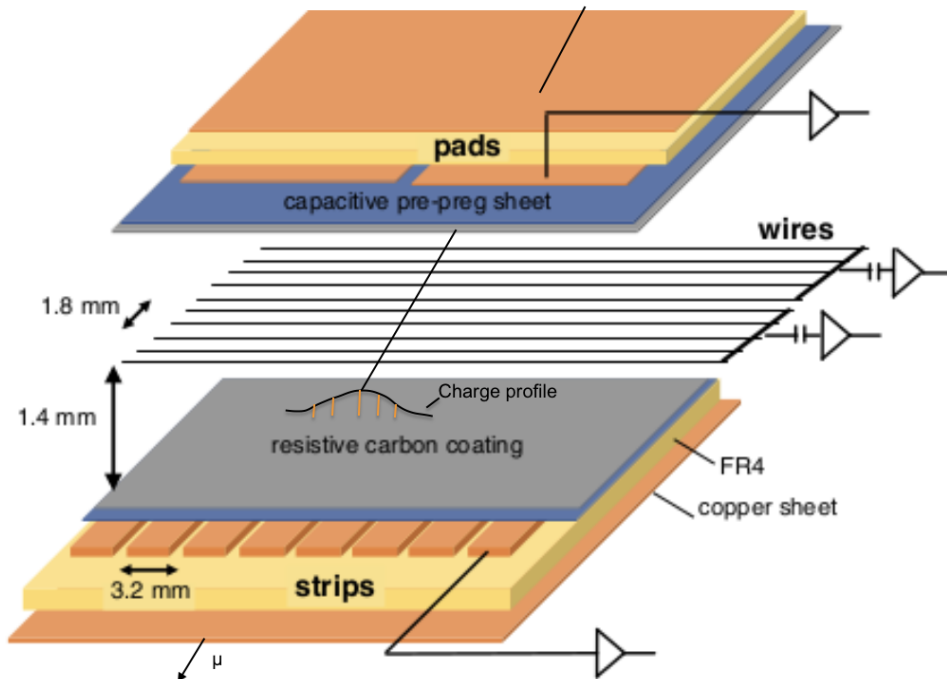


Figure 2: sTGC schematic

The cathode planes are made of a graphite-epoxy mixture with a typical surface resistivity of 100 or 200 k sprayed on a 100 or 200  $\mu\text{m}$  thick G-10 plane for the inner and outer chambers. On one side of the anode plane, perpendicular to the wires, there are copper strips that provide precise coordinate measurements. On the opposite side, copper pads are used for fast triggering. The pads occupy large rectangular areas on a

1.5 mm-thick printed circuit board (PCB), with a shielding ground layer on the reverse side. During each proton bunch crossing in the LHC, the pad occupancy is projected to be about 1.0–1.3. Both the strips and pads serve as readout electrodes. A 3-out-of-4 coincidence of the pad signals is used to identify muon tracks that approximately point back to the interaction point. These pads also define a region of interest, indicating which strips must be read out to obtain a precise coordinate for online track reconstruction. The wire readout provides the azimuthal coordinate of the muon trajectory while the strips measure the image charge induced on the wires in the y-axis, as seen in Fig.3. A gas mixture of 55% CO<sub>2</sub> and 45% n-pentane is used for operation. There are six different quadruplet sizes; three each for the large and small sectors. As shown in Fig. 1, each quadruplet has a trapezoidal shape with surface areas ranging between 1m<sup>2</sup> and 2m<sup>2</sup> [5].

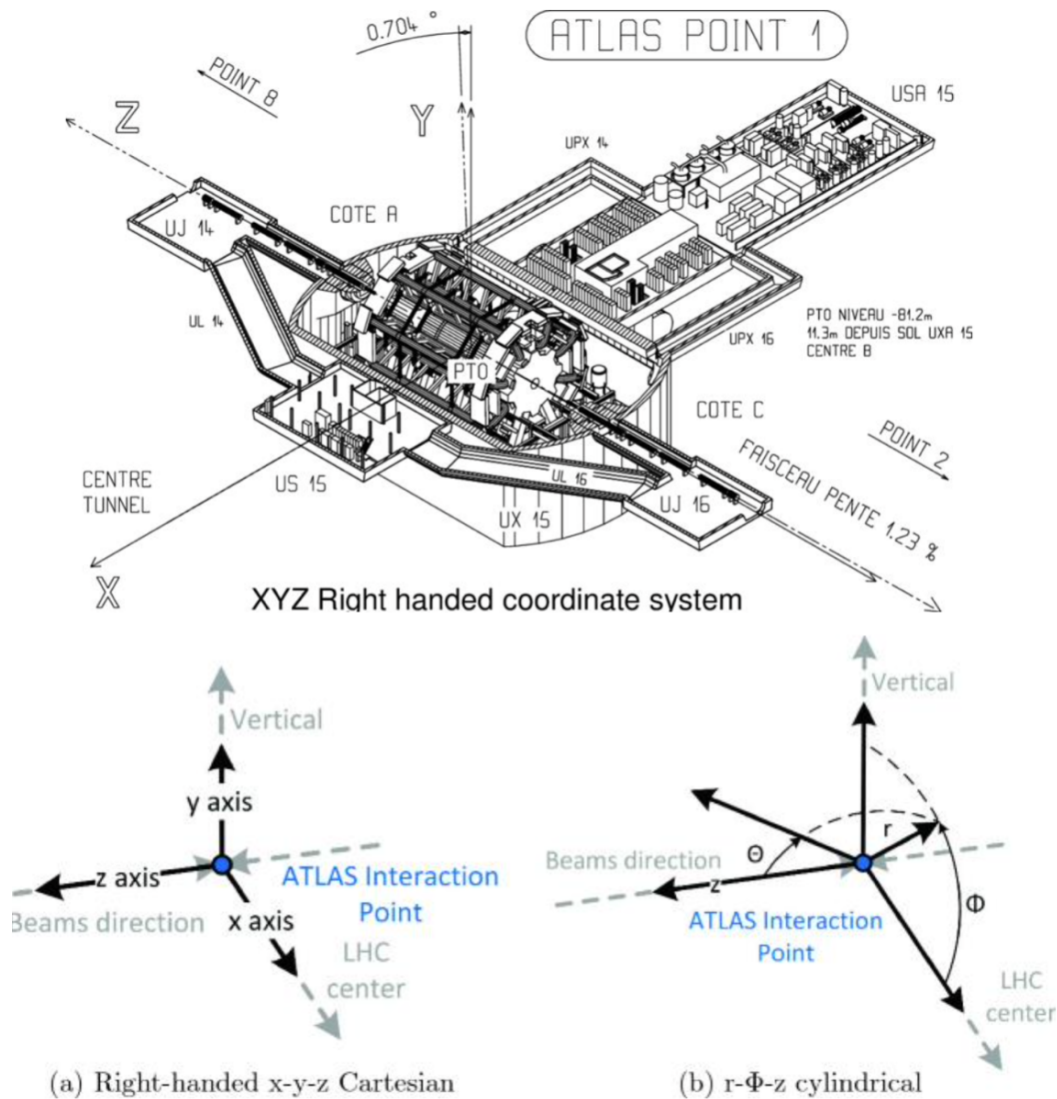


Figure 3: ATLAS Coordinate Systems

## 2.2 Strip Geometry and Readout

This project specifically analyzed the strip hit measurements from the sTGCs, which provides the positional component of incoming muons. Each readout plane is segmented into radially oriented copper strips, which lie perpendicular to the y-axis to provide precise spatial information, as shown in Fig. 4.

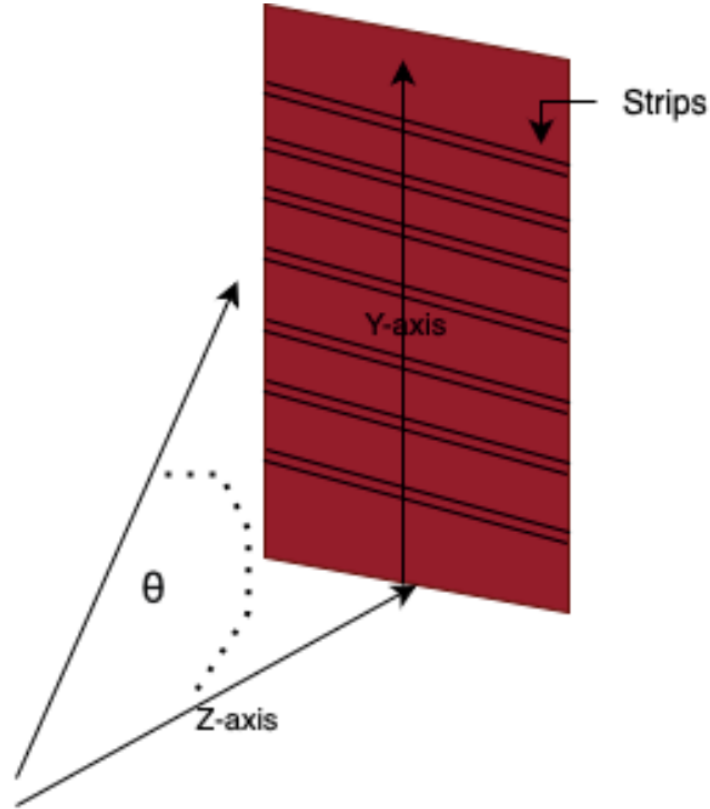


Figure 4: Strip orientation with respects to the ATLAS coordinates

The strips are normally spaced with a pitch of around 3 mm in order to balance manufacturing constraints and obtain the desired  $100 \mu\text{m}$ -level resolution [5, 6]. The current resolution is at  $200 \mu\text{m}$ . These strips reside on cathode boards, while an anode wire plane sits in the same gas gap, as seen in Fig 2. As charged particles (e.g., muons) traverse the chamber, they ionize the gas, and the resulting electrons move towards the high electric field near the wire [2]. This influx of electrons causes an avalanche whose electric field includes charges on the nearby cathode strips. As the avalanche drifts, the localized signal can be distributed across adjacent strips in a process known as charge sharing [7]. The signal is recorded by specialized front-end ASICs (e.g., VMM chips), which measure both amplitude and timing at the channel level. The strips registering above-threshold signals from the same avalanche form a cluster, and their multiplicity (the number of strips in the cluster) reflects how much the total avalanche-induced charge has spread. The sTGC strip-clusters provide measurements of the particle position in the y-direction of the plane, and their spatial resolution is directly linked to the profile of induced charge on the strips. Typically, clusters with induced charge across 3-5 adjacent strips are selected, this ensures cluster-finding performance and improved position determination. The resulting charge distribution is fitted with a Gaussian, often reaching a resolution of sub- $100 \mu\text{m}$  [5, 8]. Careful PCB design and grounding help reduce crosstalk

between closely spaced strips, while precision alignment (through fiducial markers, optical scans, and strict assembly protocols) ensures that each strip's position is correct within tens of micrometers across large trapezoidal detector planes. Together, these design choices ensure that the strips accurately measure the induced charges of the wires [8].

### 3 Theory

Beams of protons are accelerated to high energies in the LHC and brought into collision at the centre of the ATLAS detector. These collisions produce new particles, such as muons, which emerge from the interaction point in all directions. Over a billion particle interactions occur within the ATLAS detector every second [9]. The resulting particles are highly energetic and interact with the detector's active materials. Since the collision debris consists of highly charged particles, they undergo numerous elastic Coulomb interactions with the atomic electrons of the detector medium.

Excitation occurs when an atomic or molecular electron absorbs energy from a collision and jumps to a higher energy level. Ionization, on the other hand, occurs when the electron gains enough energy to escape the molecular potential entirely. As such, when a muon traverses the sTGC, it is detected through these ionization and excitation processes within the gas volume [10].

Furthermore, as these charged particles traverse the gas volume located between parallel cathode planes, they leave behind a trail of ion-electron pairs. The freed electrons then drift along the electric field lines toward the nearest anode wire. The field strength near the wire can be approximated by that of a cylindrical capacitor, Eq. 1.

$$\vec{E}(r) = \frac{V_o}{r \cdot \ln(r_a/r_i)} \hat{r} \quad (1)$$

Where  $V_o$  is the voltage applied to the anode wire,  $r$  is the radial distance from the centre of the cylindrical cathode and  $\hat{r}$  the radial unit vector. The field lines are shown in Fig. 5,

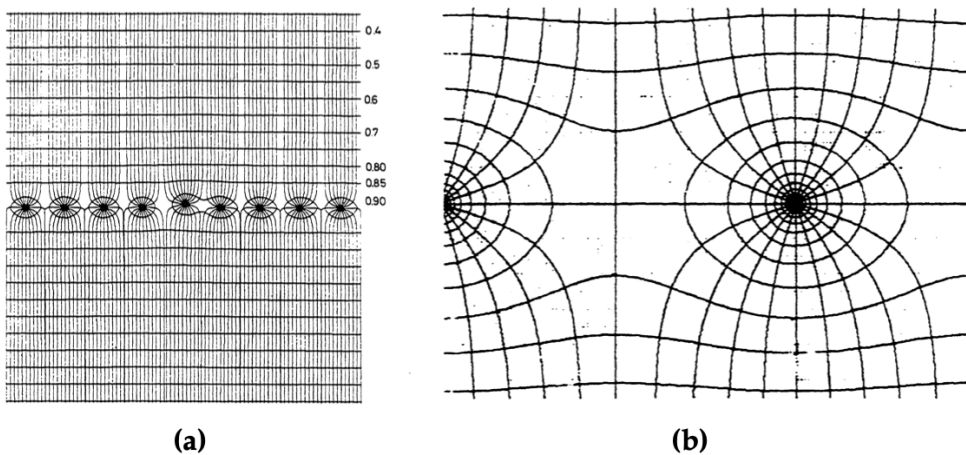


Figure 5: Electric field configuration in a multi-wire chamber: (a) global field lines and distortion from wire displacement; (b) magnified view near an anode wire. [10].

When an electron gains enough kinetic energy between collisions to exceed the ionization threshold of the gas, a secondary ionization occurs. This initiates an avalanche near the anode wire. Each avalanche induces a pulse on the anode wire, primarily due to the motion of positive ions drifting away from it. Multiple pulses are generated as successive avalanches are triggered by clusters of primary ionization electrons drifting into the high-field region one after another [11]. In itself, each wire behaves like an individual detector. Where then the position of an incident particle can be deduced from the signal induced on anode wires.

As such, the cathode strips measure the transverse spatial coordinate of a charged particle's path as it passes through the detector. When a muon or other charged particle induces an avalanche near the anode wire, a portion of the resulting signal is also induced on the segmented cathode strips. Because the induced charge spreads over multiple adjacent strips, the charge distribution can be analyzed to determine the particle's position with high precision. A centroid-finding algorithm is then applied to this distribution, allowing the reconstruction of the particle's location perpendicular to the wire direction. This method provides spatial resolution that is not limited by the strip pitch, and significantly improves the tracking accuracy compared to wire readout alone. This is can be seen in Fig. 6.

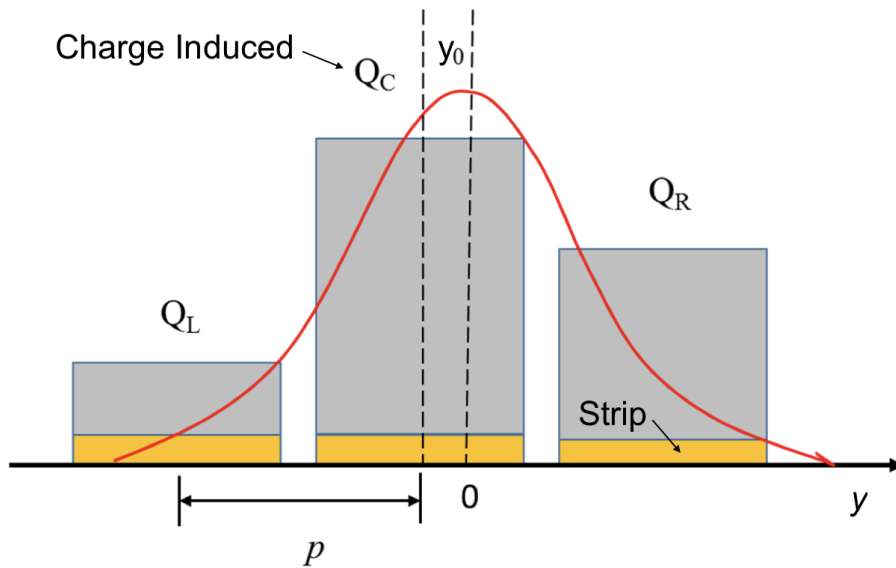


Figure 6: Charge dispersion on strips

Where  $p$  is the strip pitch, and  $Q$  is the induced charge on the left, centre and right strips [7].

## 4 Measured Variables and Methodology

This section outlines the key variables used to evaluate the performance of the sTGC detectors and the methodology applied to extract them from real and simulated data. Each quantity, such as cluster multiplicity, residuals, resolution, and pull, serves as a diagnostic of reconstruction accuracy and detector response. The procedures used to measure these variables combine analytical fits (e.g., Gaussian modeling), angle-dependent binning, and

statistical estimators. Together, these metrics provide a quantitative framework for understanding and optimizing the tracking performance of the NSW subsystem.

## 4.1 Digitization

The digitization of sTGC strip measurements refers to the process of converting the analog charge signals into discrete digital information that can be processed offline. The conversion is based on the results taken from analytical simulations and/or actual data that are then implemented as parameters or distributions [12].

### 4.1.1 Cluster Multiplicity

As previously mentioned, a cluster is defined as a set of hits in contiguous strips, with hit times that are separated by less than 12.5 ns [13]. Cluster multiplicity refers to the total number of strips activated and subsequently digitized for a single cluster. Based on simulation studies, clusters are expected to typically consist of signals from 3 to 5 adjacent strips. For cluster multiplicities equal or greater than 3, the Caruana method used to reconstruct the cluster, serving as a Gaussian fit used for sTGC [14, 10]. For clusters outside this range, a weighted mean is used instead. Both methods are further explained in 4.2.1. Since clusters provide the position in the y direction, the average size of the cluster varies with the muon angle theta,  $\theta$ , as it passes through the detector, as seen in Fig. 7. Cluster multiplicity is a valuable reconstruction parameter because clusters generally form close to the impact point of the muon. By analyzing how many strips fire together during an event, the position estimate can be refined, and potential issues such as electronic noise or cross-talk can be identified and mitigated [10].

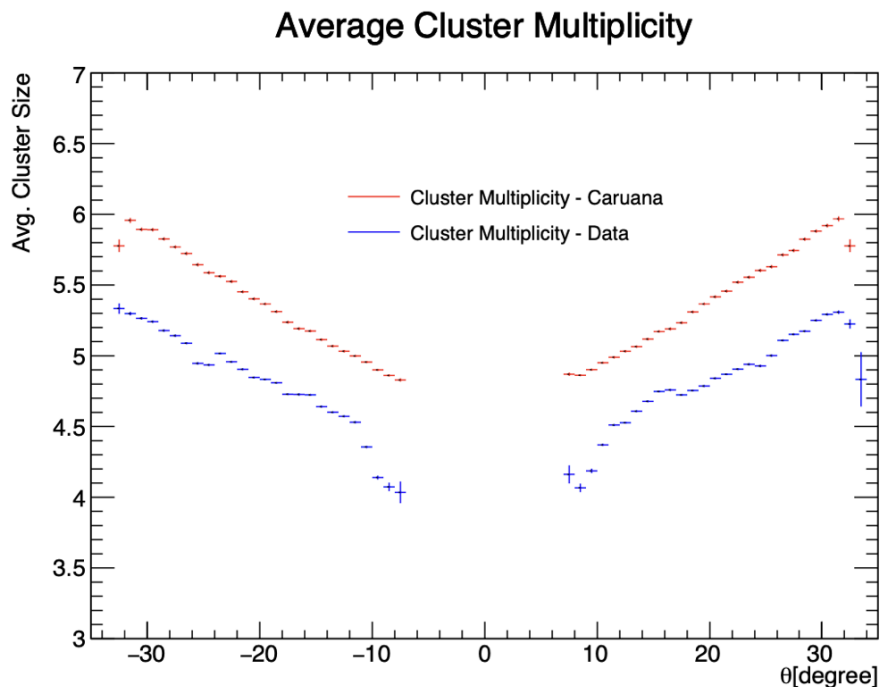


Figure 7: Average Cluster size per muon angle theta [15]

### 4.1.2 Truth Residual

The truth residual is defined as the difference between the reconstructed hit position and the true position, as expressed in Eq.2:

$$Residual_{truth} = y_{reco} - y_{truth} \quad (2)$$

Since the true hit position is only produced by Monte Carlo simulations, truth residuals cannot be obtained from real collision data. Analyzing the truth residual provides a direct measure of the reconstruction accuracy and allows the identification of outliers, which may result from noise or misidentified clusters. This analysis is essential for validating that local pattern-recognition algorithms and cluster-based reconstruction methods are producing consistent and high-precision spatial coordinates for muon tracking. An example of the truth residual distribution is shown in Fig.8

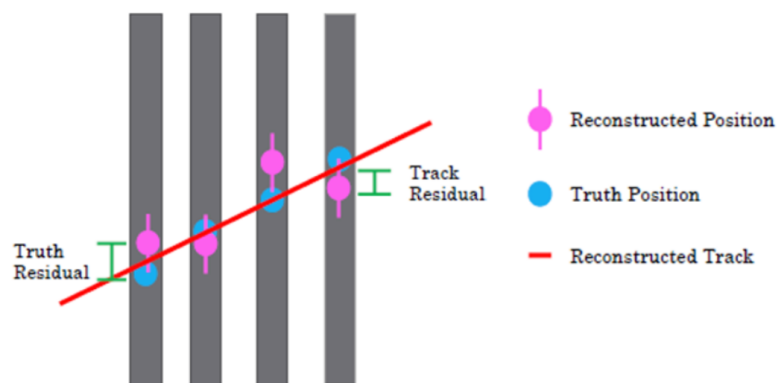


Figure 8: Comparison of Truth and Reconstructed Positions Along the Track

An example of a 2D histogram of truth residual per incoming angle obtained from simulated is shown in Fig.2. The distribution is centered around 0mm, indicating that the reconstructed hit positions are generally well-aligned with the true simulated track positions.

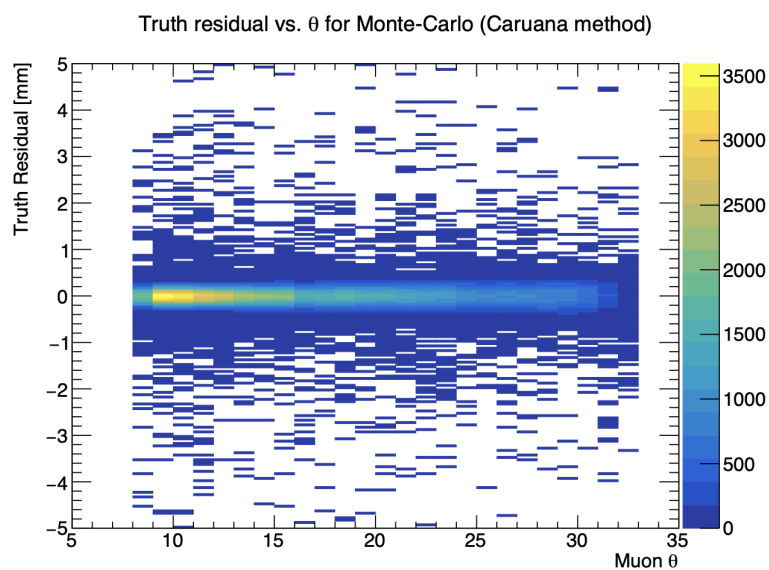


Figure 9: Truth Residual per Angle [15]

## 4.2 Reconstruction

Reconstruction refers to the process of recreating the trajectory or track of a muon as it traverses the detector. In the case of sTGC strip data, this involves converting clustered hit information (digitized charge distributions) into precise estimates of the muon's track parameters within the ATLAS end-cap. Track reconstruction is independently determined in the y-z and x-z planes using strip and wire data from the three sTGC readout layers. Localized pattern recognition algorithms are employed to identify the muon's impact points on the sTGC planes and combine these points across multiple sectors to form a coherent track segment. A Gaussian or a centroid fit is then applied to each cluster to extract the position measurements used to define the muon track candidates [12].

### 4.2.1 Error Parametrization

There is currently no universally established theoretical model that describes the exact distribution of induced charge on the strips. As a result, empirical methods are typically used to approximate the charge profile in a realistic manner. In practice, the charge distribution is observed to exhibit a bell-shaped profile and is therefore commonly modeled using a Gaussian function. The Caruana and centroid methods were both used as error parameterizations to describe the charge profile. As such, these methods were compared against each other to determine which provided a better resolution for the track residual as discussed in Section 4.2.2.

The centroid method serves as a weighted mean estimator and is given by Eq.3 and 4 which are the mean and variance:

$$\hat{\mu} = \frac{\sum_{i=1}^N q_i x_i}{\sum_{i=1}^N q_i} \quad (3)$$

$$\hat{\sigma}^2 = \rho^2 \cdot \frac{\sum_{i=1}^N q_i^2}{\left(\sum_{i=1}^N q_i\right)^2} \quad (4)$$

Where  $q_i$  is the charge,  $x_i$  is the position of the  $i$ th strip, and  $\rho$  is the the single strip resolution. The centroid of a cluster is defined as the weighted average position of the strips in the cluster, where the weights correspond to the induced charge on each strip. In the context of sTGC reconstruction, the centroid provides an estimate of the particle's hit position along the strip plane. While centroid-based reconstruction is computationally efficient, it is sensitive to charge fluctuations and outliers, particularly in low-multiplicity clusters or those affected by noise [16].

The Caruana method is conceptually similar to the centroid approach but offers greater robustness with less bias. In addition, it provides a more detailed characterization of the charge distribution shape, making it better suited for precision reconstruction in complex detector environments. Caruana's algorithm is based on the fact that a Gaussian function can be expressed as the exponential of a quadratic function. This fact is used to derive a simple yet effective technique for estimating the parameters of a Gaussian distribution, offering improved accuracy over basic centroid-based methods [17]. Caruana's equations are shown below:

$$\chi^2 = \sum_{i=1}^N \frac{(\ln(\hat{q}_i) - a - bx_i - cx_i^2)^2}{\nu^2} \quad (5)$$

$$\begin{bmatrix} N & \sum_{i=1}^N x_i & \sum_{i=1}^N x_i^2 \\ \sum_{i=1}^N x_i & \sum_{i=1}^N x_i^2 & \sum_{i=1}^N x_i^3 \\ \sum_{i=1}^N x_i^2 & \sum_{i=1}^N x_i^3 & \sum_{i=1}^N x_i^4 \end{bmatrix} \begin{bmatrix} a \\ b \\ c \end{bmatrix} = \begin{bmatrix} \sum_{i=1}^N \ln(\hat{q}_i) \\ \sum_{i=1}^N x_i \ln(\hat{q}_i) \\ \sum_{i=1}^N x_i^2 \ln(\hat{q}_i) \end{bmatrix} \quad (6)$$

$$\hat{\mu} = \frac{-b}{2c} \quad (7)$$

$$\hat{\sigma}_\mu = \frac{\nu}{2c} \sqrt{\frac{1}{\gamma_2} + \frac{b^2}{c^2} \cdot \frac{\gamma_0}{\gamma_0\gamma_4 - \gamma_2^2}} \quad (8)$$

The Caruana algorithm is computationally efficient, as it is non-iterative. However, its primary drawback is a significant loss in accuracy in the presence of noise. This sensitivity arises from the algorithm's use of the logarithm of the input data, which becomes problematic when the observed values include zeros, leading to undefined or erroneous results [18].

As such, the standard error on the cluster centroid,  $\hat{\sigma}_\mu$ , provides the uncertainty in millimetres on the cluster's central position. This error applies to pads, strips, and wires, each serving a distinct function: strips measure the track in the local y-direction, wires measure the track in the local x-direction, and pads trigger the readout [10]. From the Caruana method,  $\hat{\sigma}_\mu$  is obtained from the positions of the activated strips relative to the cluster centre, the recorded charge on each strip, and an angular dependency  $\nu(\theta)$ . The function  $\nu(\theta)$  depends on the incident muon angle and incorporates both the positional resolution and the angular resolution parameters, P and A [10, 15]. The error is given by Eq. 9:

$$\nu(\theta) = \sqrt{P^2 + (A \cdot \tan(\theta))^2} \quad (9)$$

Where  $\theta$  is the incident muon angle, P is the positional resolution and A is the angular resolution. The positional error affects the position of the centre of the error while the angular component affects the width of the error [10, 15].

### 4.2.2 Track Residual

The track residual is the difference between the reconstructed position and the measured hit, as shown below:

$$Residual_{track} = y_{reco} - y_{track} \quad (10)$$

The track residual is obtained by reconstructing the hits from strip data and applying a track fit using either the Caruana or centroid method. Once the track has been fitted, it is extrapolated to each detector layer, either in local or global coordinates. The residual is then calculated as the difference between the extrapolated track position and the digitized hit position within each gas gap. Similar to the truth residual, the following diagram further demonstrates the differences between the residuals.

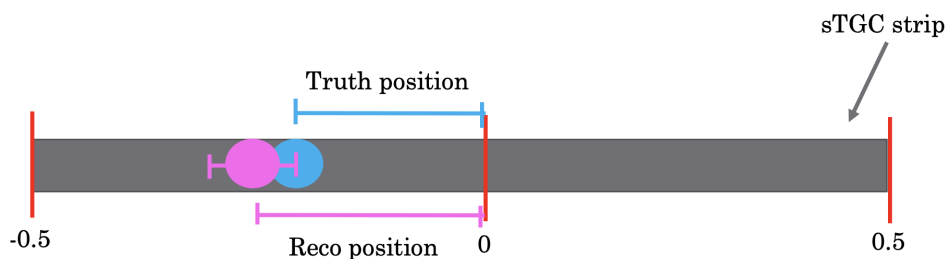


Figure 10: Relative strip position defined from -0.5 (bottom) to 0.5 (top) of the nearest strip centre

This project mainly focused on residual track from real data and similar to Fig. 9, a 2D histogram was produced from the track residual, as shown below:

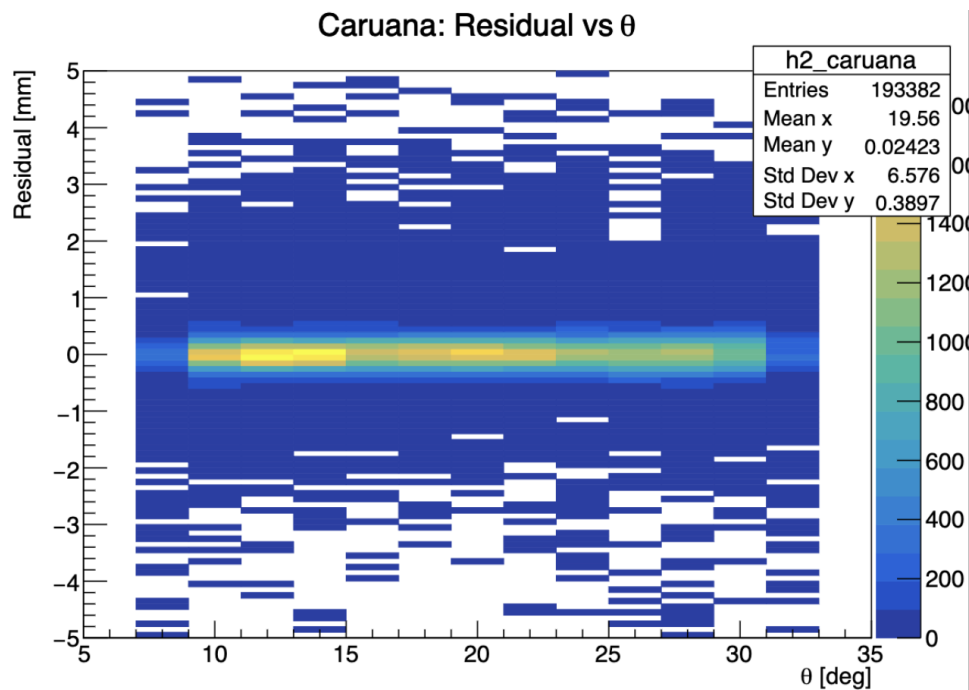


Figure 11: Track residual per angle from real collision data

### 4.2.3 Resolution

After these residuals are plotted in a histogram and separated into bins corresponding to different reconstructed track angles  $\theta$ , the individual angle bins can be plotted with respects to the residual range and fitted with a Gaussian, as shown in Fig.12.

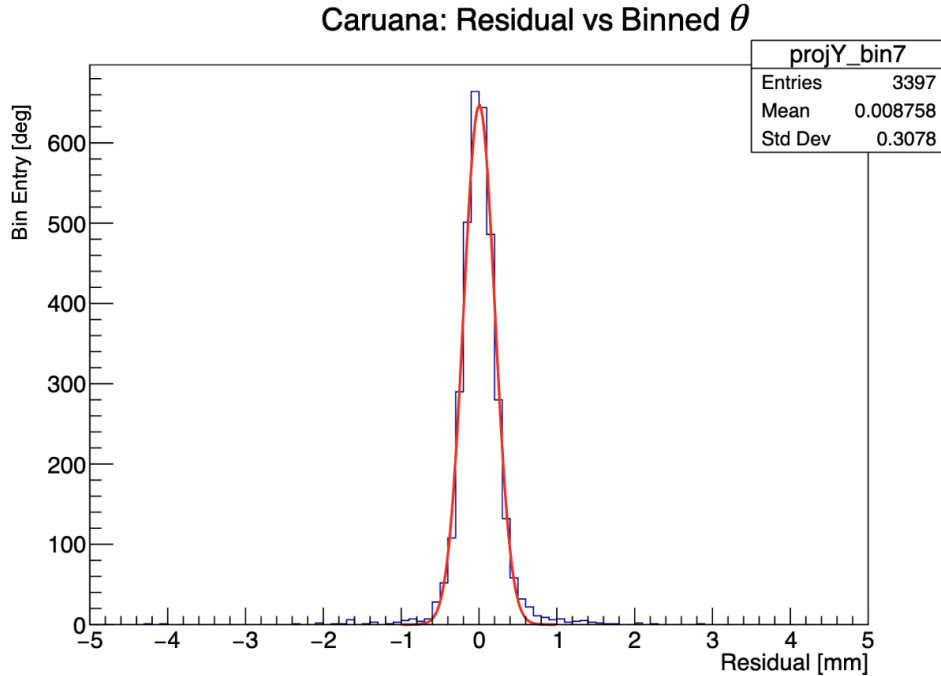


Figure 12: Track residual per Binned  $\theta$

The width of each distribution serves as a biased estimate of the intrinsic spatial resolution. This width reflects how accurately the detector and its reconstruction algorithms can localize the true particle position. By analyzing residuals across a large sample of events, the overall performance of the detector and the reliability of the reconstruction process can be effectively evaluated [10]. As such, the sTGC resolution is obtained from the width of the Gaussian function fitted to the track residual distribution, with the associated uncertainty taken as the error on the standard deviation [10, 15, 19]. To obtain a reliable Gaussian fit, the residual domain is often symmetrically restricted around zero. While this helps eliminate outliers, it may introduce a bias in the standard deviation. Additionally, the cluster profile is affected by the incident muon angle, which directly impacts the resolution. Fig. 13 displays the resulting resolution curve.

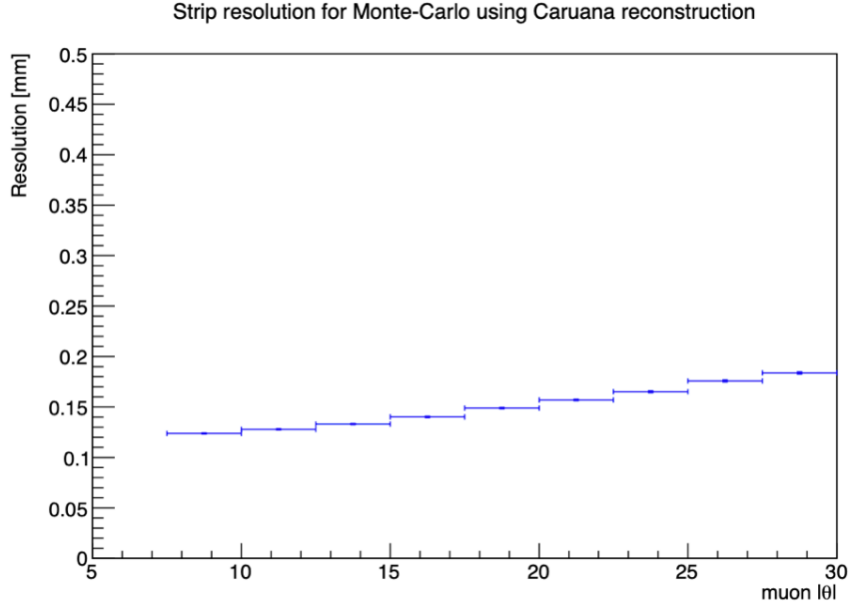


Figure 13: Strip resolution per muon angle [15]

Furthermore, two key components contribute to the overall resolution: angular resolution and positional resolution. The angular resolution refers to the effects of the incident muon angle on the cluster size, while the positional the distance between strips. Although these two parameters are independent of each other, they both affect the mean of the cluster during reconstruction [10, 15, 19]. As a result, they also contribute to the uncertainty on the mean position, which in turn affects the calculated pull. The cluster width,  $\sigma$ , is related to the tangent of the incident angle scaled by a proportionality constant  $A$  as described in Eq. 11 :

$$\sigma = A \cdot \tan(\theta) \quad (11)$$

The quadrature sum of these resolutions give the theta-dependence term,  $\nu(\theta)$  as seen in Eq.9.

#### 4.2.4 Pull

The pull is a dimensionless quantity used to evaluate how well the reconstruction model describes the data. It is defined as the residual divided by its estimated uncertainty, effectively acting as a normalized residual. For a well-calibrated model, the pull distribution should follow a standard normal distribution,  $N(0,1)$ , meaning it has a mean of zero and a standard deviation of one. A non-zero mean in the pull distribution indicates a systematic bias in the reconstruction i.e., the reconstructed positions are consistently offset from the true values [20]. Similarly, if the width (standard deviation) deviates from one, it reflects a mismatch between the modeled uncertainties and the true spread of the residuals. Specifically, a width greater than one implies that the uncertainties are underestimated, while a width less than one indicates they are overestimated [21]. Therefore, verifying that the pull distribution adheres to  $N(0,1)$  is a practical method for assessing both the absence of bias and the accuracy of the uncertainty estimation, such as that derived from the Caruana method. The pull can be computed for both track residuals and truth residuals as shown below:

$$\text{Pull}_{\text{track}} = \frac{\text{Residual}_{\text{track}}}{\hat{\sigma}_{\mu}} \quad (12)$$

$$\text{Pull}_{\text{truth}} = \frac{\text{Residual}_{\text{truth}}}{\hat{\sigma}_{\mu}} \quad (13)$$

Ideally, the pull should be independent of the incident muon angle and consistently exhibit a mean of zero and a width of one across all angular bins. This behavior confirms that the reconstruction process introduces no systematic offset and that the associated error model is correctly parameterized. Fig.19 shows a typical pull distribution.

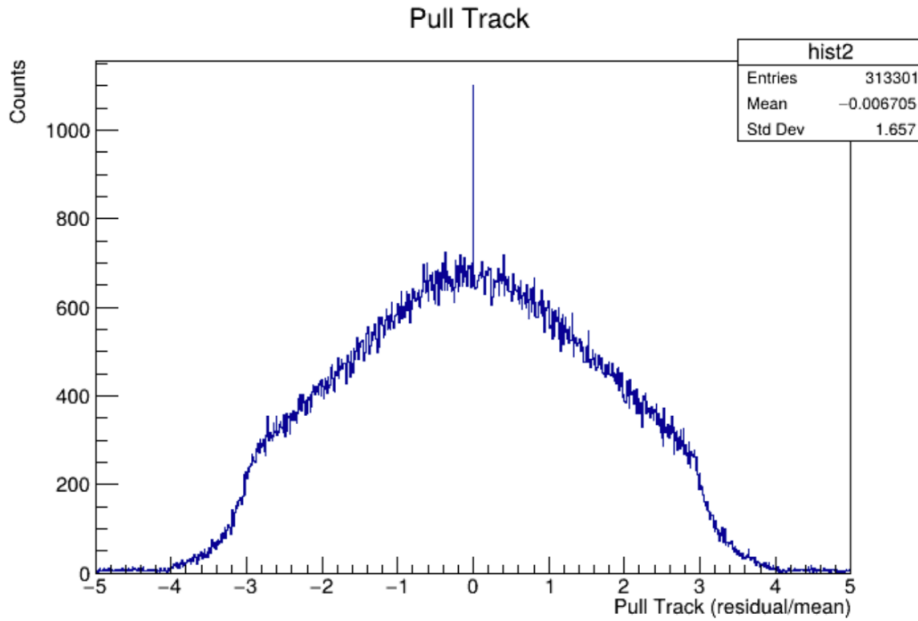


Figure 14: Monte-Carlo strip pull track per events

Furthermore, the standard deviation of the pull distribution also referred to as the RMS pull, is also a crucial diagnostic. It indicates whether the modeled uncertainties accurately reflect the true spread of the residuals. An RMS pull value close to 1 suggests that the reconstruction algorithm's estimated errors are well-calibrated and consistent with the actual variation in the measured hit positions. If the RMS pull is significantly greater than 1, it implies that the uncertainties are underestimated, meaning the observed spread is larger than what the model predicts. Conversely, a value much less than 1 indicates that the uncertainties are overestimated. In essence, while the mean of the pull distribution reveals any systematic bias (i.e., a consistent offset), the RMS pull assesses the accuracy of the uncertainty model itself.

To generate an RMS pull plot, events are binned according to the incident muon angle, and the pull is calculated for each event in the bin. The RMS of these pulls is then computed and plotted as a function of angle, illustrating how well the error model performs across different angular regions. Thus, the mean and RMS pull together provide a comprehensive evaluation of the reconstruction model: the former checks for bias, while the latter verifies whether the uncertainty estimates are properly calibrated across the full operational range of the detector [21]. Fig. 15 displays the RMS pull as a function of incident angle based on Monte Carlo simulation results.

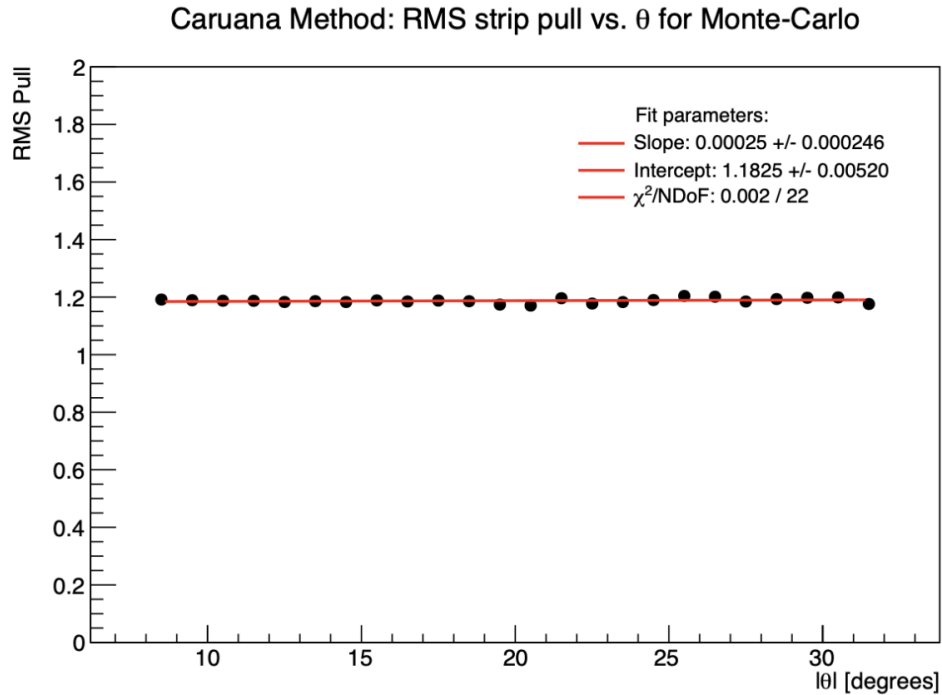


Figure 15: RMS pull per muon angle [15]

#### 4.2.5 Efficiency

Efficiency quantifies the fraction of true events that are successfully detected and reconstructed. For a given detector layer and muon, an event is considered efficient if a cluster is found within 5mm of the reconstructed track position. The layer efficiency is calculated by averaging this detection rate over all muons passing through that layer. The overall detector efficiency is then obtained by averaging the efficiencies across all layers. Efficiencies are evaluated separately for pads, strips, and wires, and are measured on both side A and side C of the ATLAS detector. For Monte Carlo simulations, the expected efficiency is greater than 95% [15].

## 5 Development and Implementation

### 5.1 1st Term

The initial part of the term focused on developing the necessary skills to read, write, and modify code using the ROOT framework. ROOT is the primary tool used for reconstruction due to its capacity to efficiently handle large volumes of data. Following this, effort was dedicated to understanding the underlying physics associated with each plot generated through the code. This included familiarizing oneself with the geometry and dimensions of the ATLAS detector, as well as the electrodynamics governing the sTGC subsystem. Custom scripts were also written to visualize and reproduce the plots referenced throughout this report. Furthermore, a tuning decision for the 2024 analysis was made. In this context, tuning refers to selecting appropriate values for the positional and angular resolution parameters  $P$  and  $A$  in Eq. 9.

The goal of this analysis was to determine which set of parameters would yield better spatial resolution and a pull distribution consistent with the ideal normal distribution  $N(0,1)$ . Two sets of tunings were compared: one that overestimated the reconstruction uncertainty, and another that underestimated it. Despite their differences, both tunings produced pull values close to 1. The selected values are summarized in Table 1.

Table 1: Tuning parameters with corresponding values

Parameters	Tuning 1	Tuning 2
$P$ (mm)	0.15	0.0949
$A$ (mm)	0.5	0.305

The main distinctions between the tunings, is that Tuning 1 overestimates the error while Tuning 2 underestimates it.

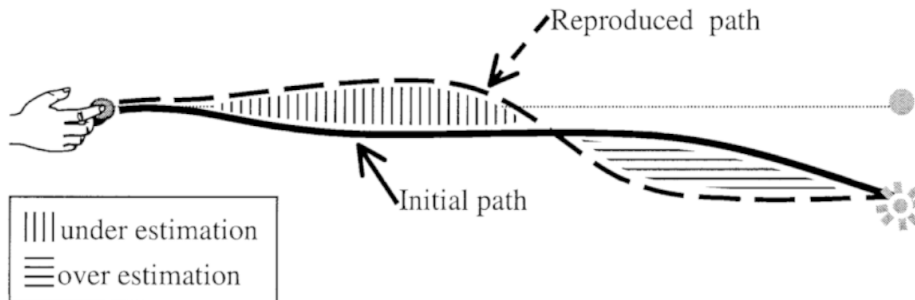


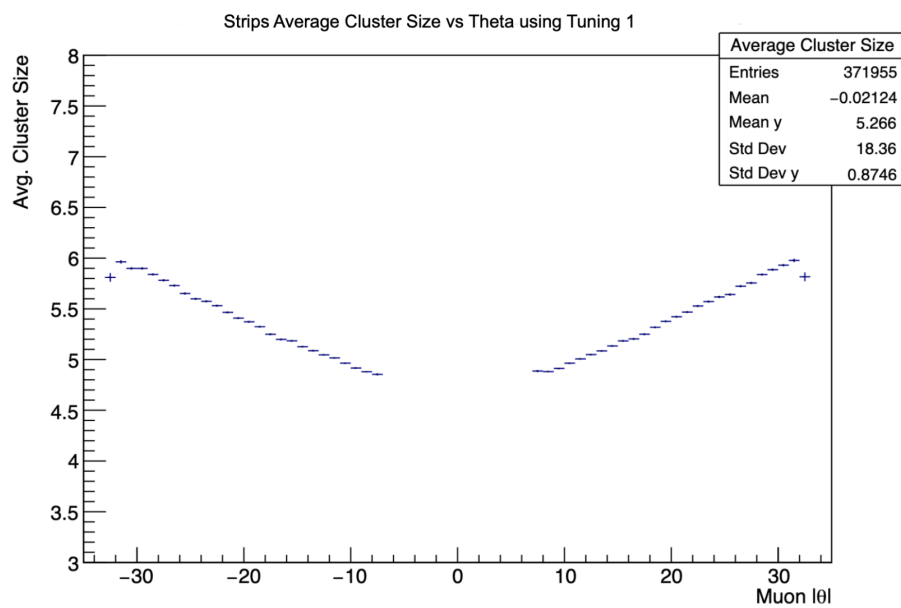
Figure 16: Depiction of error estimation [22]

Accurately estimating the error during track reconstruction is essential for developing reliable algorithms that reflect the true detector performance. Both over- and underestimation can significantly impact the quality of the reconstructed measurements, leading to biased interpretations or reduced sensitivity. These effects are illustrated in Fig. 16. For the analysis, several key performance metrics were evaluated for both tunings, including efficiency, cluster multiplicity, spatial resolution, and the pull distribution. As previously noted, the expected efficiency for Monte Carlo simulations is at least 95%. As shown in Table 2, both Tuning 1 and Tuning 2 exceed this threshold, indicating that each configuration meets the basic performance requirements in terms of hit detection.

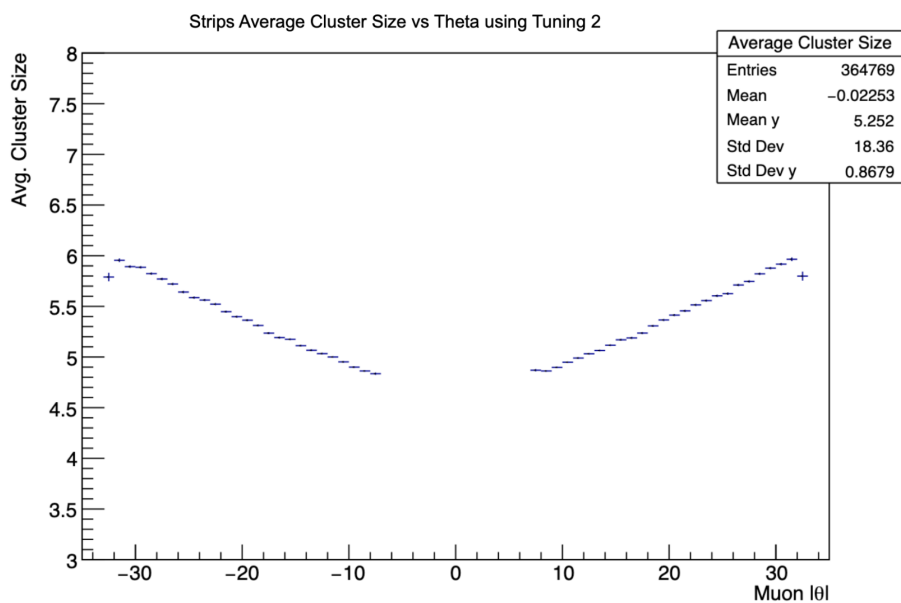
Table 2: Efficiencies (%) for each Tuning

Parameters	Tuning 1		Tuning 2	
	A	C	A	C
Strips	95.29	95.29	95.30	95.29
Wires	97.00	96.89	96.99	96.88
Pads	98.86	98.83	98.84	98.83

The strip multiplicities for each tuning are shown in Fig. 17. The values exhibit only minor variations between the two configurations, as a result their standard deviations are effectively equivalent.



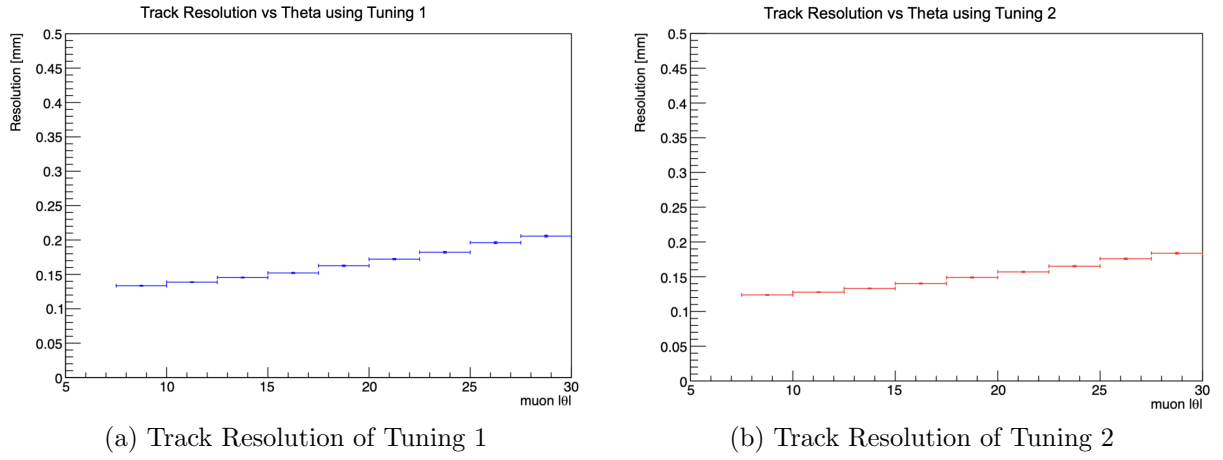
(a) Strip Multiplicity with Tuning 1



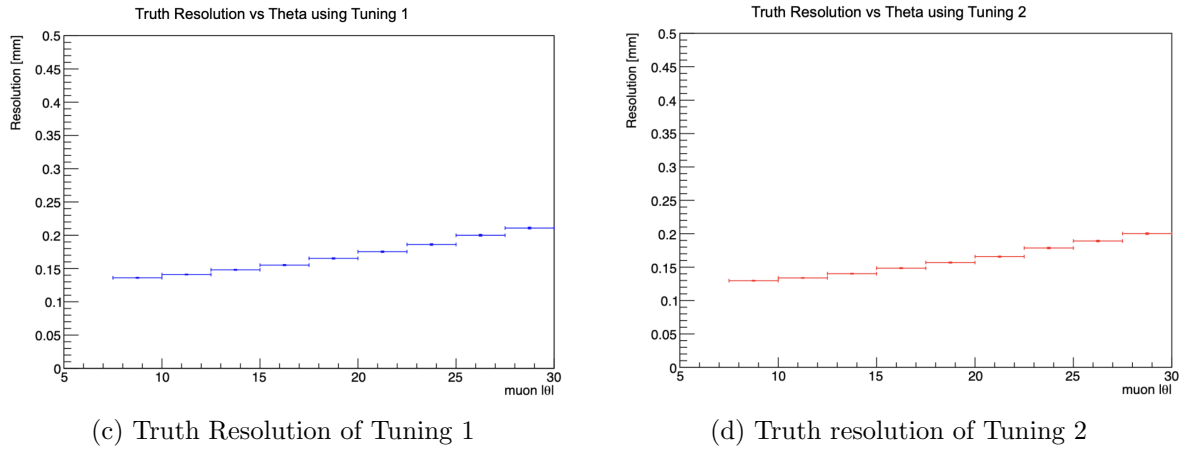
(b) Strip Multiplicity with Tuning 2

Figure 17: Strip Multiplicities per incident angle of both Tunings

Both truth and track resolutions of each tuning are also seen to only vary slightly in values. As shown in Fig. 18.



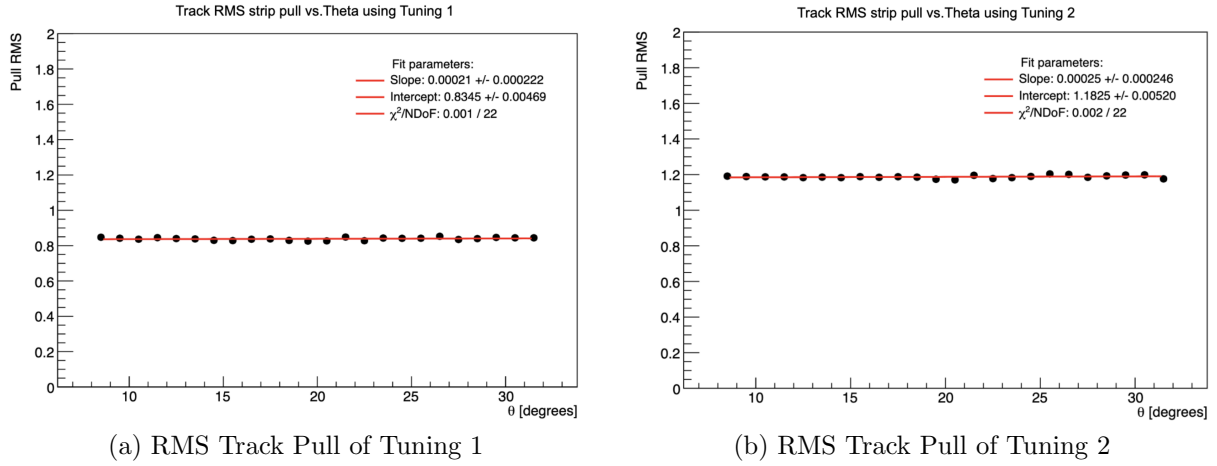
Application of Tunings for track Resolution



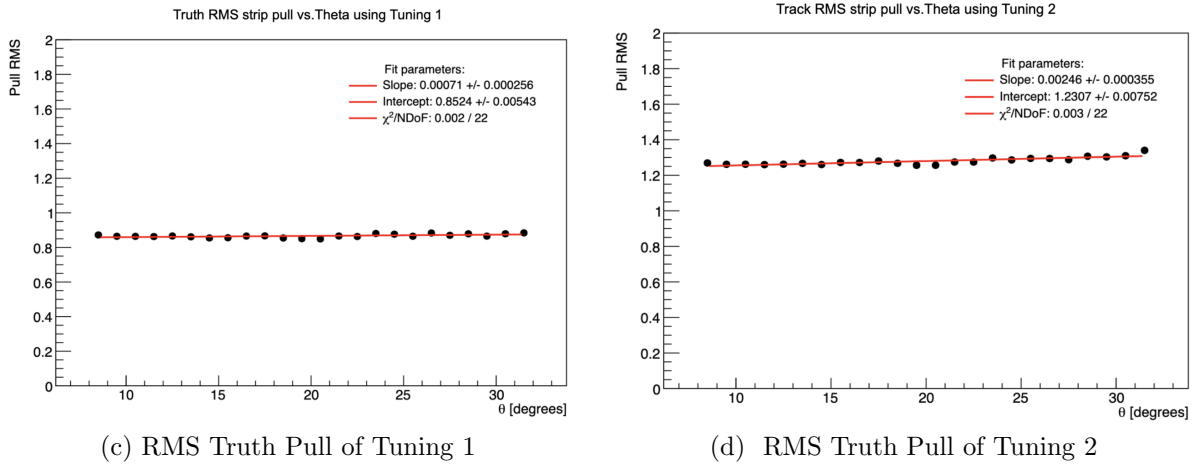
Application of Tunings for truth resolution

Figure 18: Comparison of track and truth resolution as a function of muon angle for Tuning 1 and Tuning 2. Top: track resolution; bottom: truth resolution.

Although both tunings yield similar efficiencies, multiplicities, and resolution values, they are not equivalent. Even small variations between them can significantly influence the resulting pull distributions. As previously discussed, the two tunings estimate reconstruction error differently, which is reflected in the pull behavior shown in Fig. 19. Both the track and truth RMS pull exhibit slight but meaningful differences depending on the chosen tuning.



Application of Tunings for Track RMS Strip Pull



Application of Tunings for Truth RMS Strip Pull

Figure 19: Comparison of RMS Strip pull as a function of muon angle for Tuning 1 and Tuning 2. Top row: track RMS pull ; bottom row: truth RMS pull.

It is evident that Tuning 1 yields an RMS pull slightly less than one, while Tuning 2 results in an RMS pull greater than one. Neither tuning is perfectly optimal because both deviate from the ideal RMS pull of unity. However, Tuning 1 was ultimately selected for use in this analysis. This choice reflects a deliberate preference for overestimating rather than underestimating the reconstruction error.

Overestimating uncertainty offers a conservative approach that reduces the risk of false positives by avoiding the misidentification of noise or statistical fluctuations as genuine signals. It also provides a buffer against unaccounted systematic uncertainties or inconsistencies in the sTGC detector performance. For instance, due to inefficiencies in the readout system, not all strips activate during a given event, leading to potential data loss and reduced hit identification accuracy. While overestimating error may reduce sensitivity to subtle effects and necessitate larger datasets to achieve statistical significance, it ensures that reconstruction remains robust and reliable. When paired with ongoing calibration and refinement of the reconstruction pipeline, this conservative strategy supports the production of credible, high-quality results.

## 5.2 2nd Term

In the second half of the term, only the track residual was analyzed for both real and simulated data and Tuning 1 was implemented. Subsequently, a comparative study was conducted to evaluate the effectiveness of the Caruana method versus the centroid method to determine which provided a better resolution. Fig. 20 displays the overlay of the track residual parametrized with Caruana and centroid.

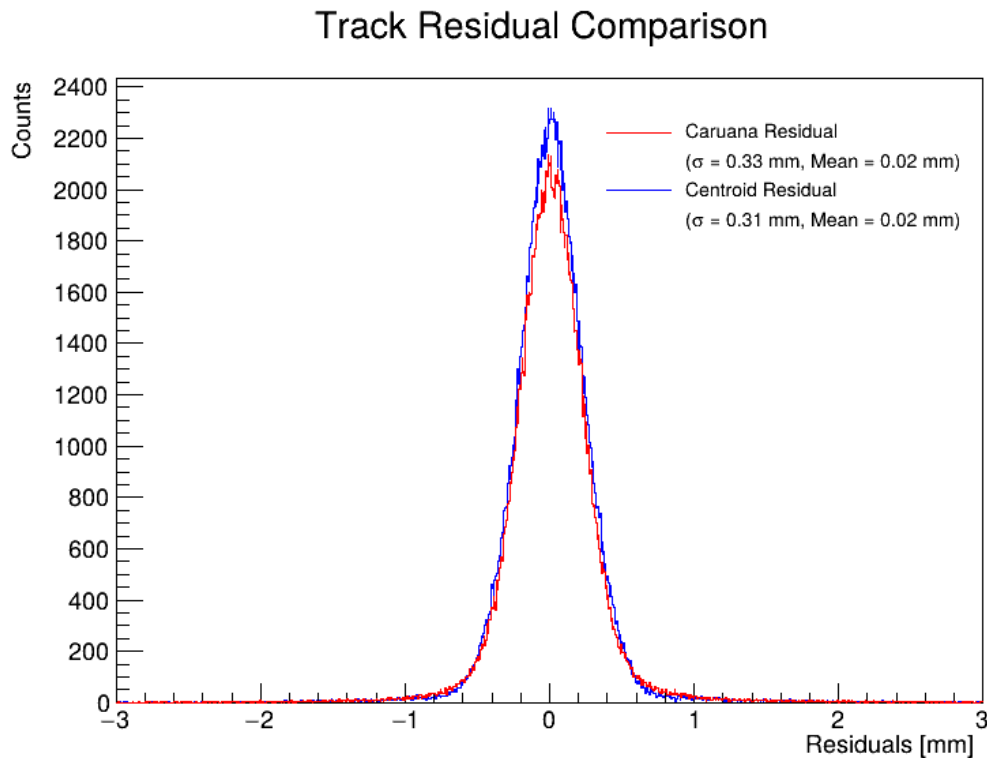
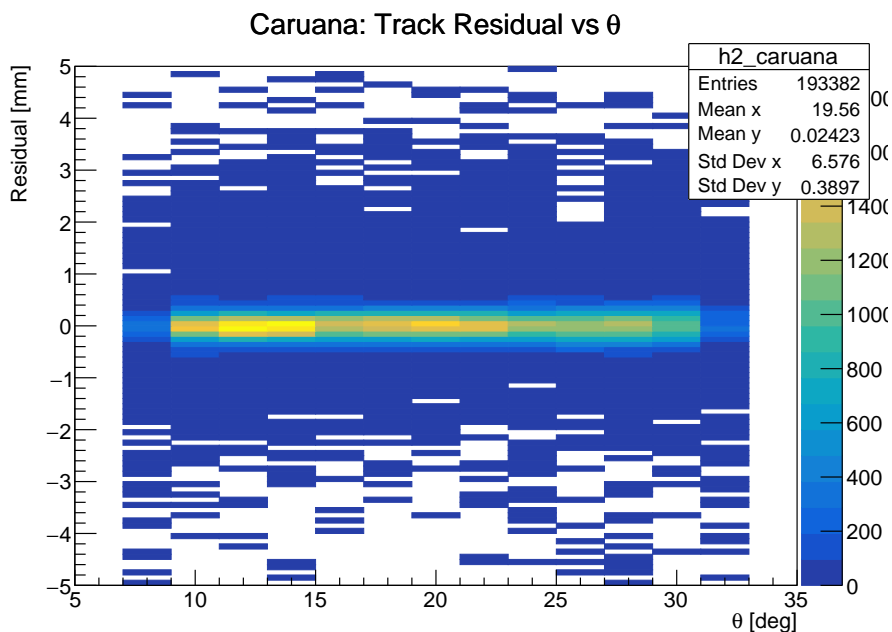
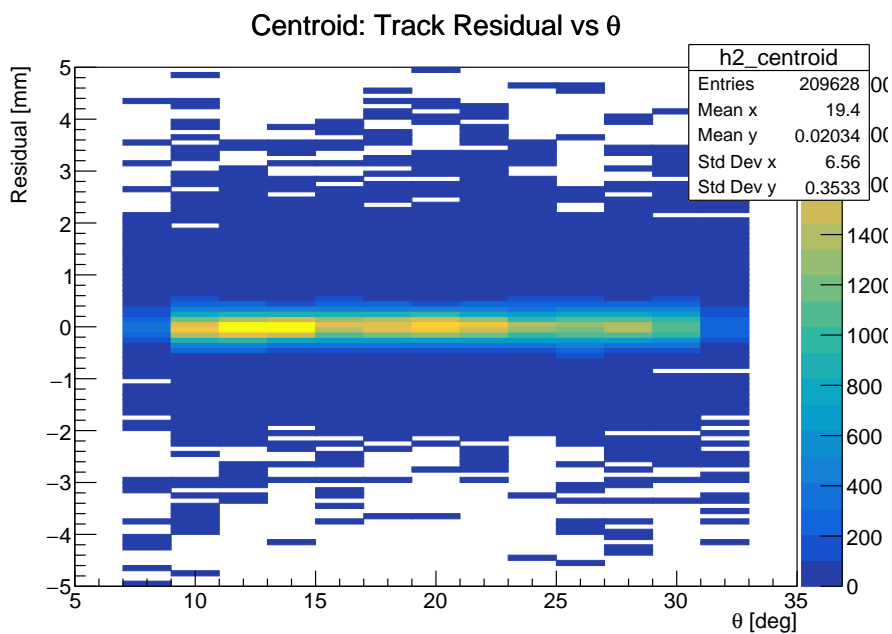


Figure 20: Comparison of Caruana and Centroid Methods for Track Residual

Furthermore, 2D histograms of the track residual as a function of incident angle were produced. This was done to extract binned data within specific angular ranges and to individually plot the residual distributions for each bin.



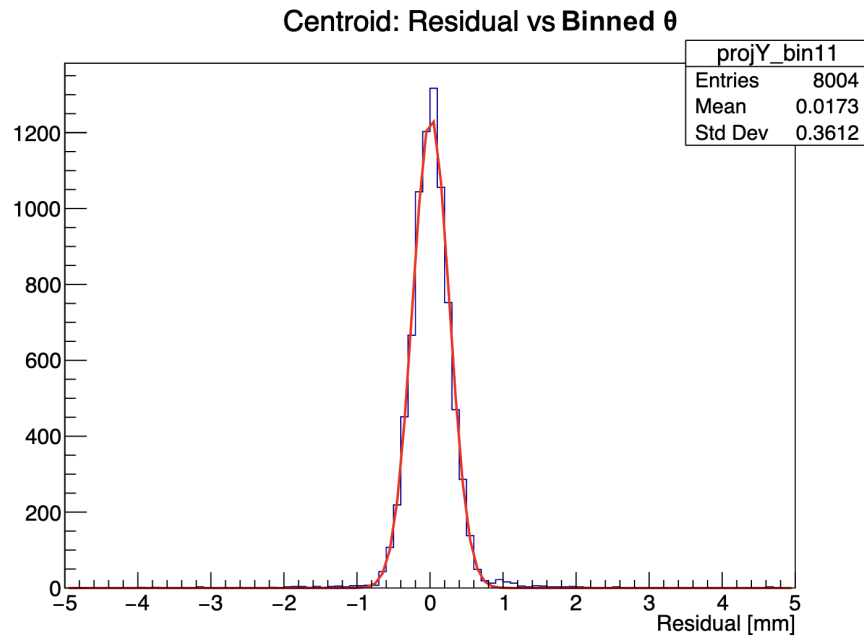
(a) Track Residual with Caruana per angle



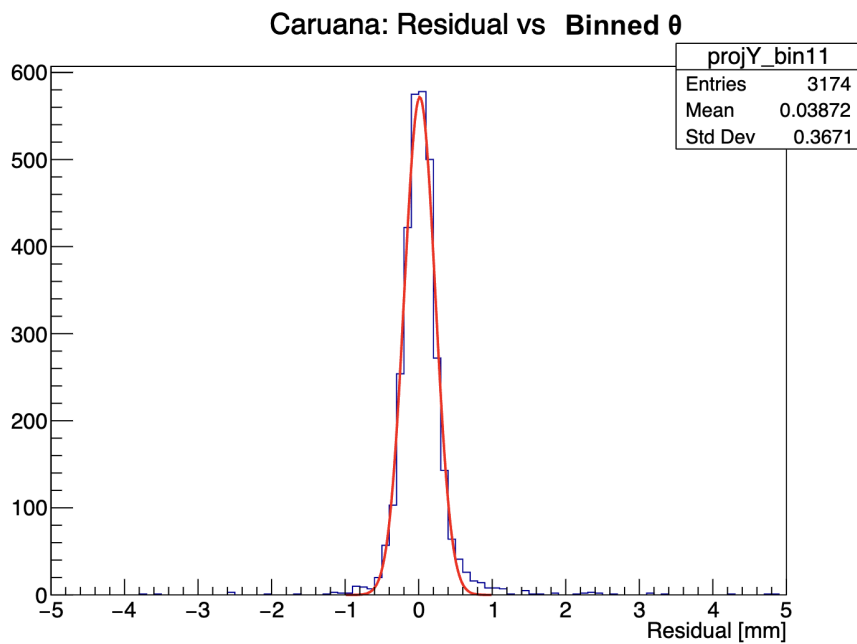
(b) Track Residual with centroid per angle

Figure 21: 2D Distribution of Track Residuals vs. Incident Angle: Caruana (a) vs. Centroid (b)

As mentioned, from the 2D plots the binned data entries were plotted against the residual and fitted with a Gaussian, which can be seen in Fig. 22.



(a) Binned angle entry per residual with Centroid



(b) Binned angle entry per residual with Caruana

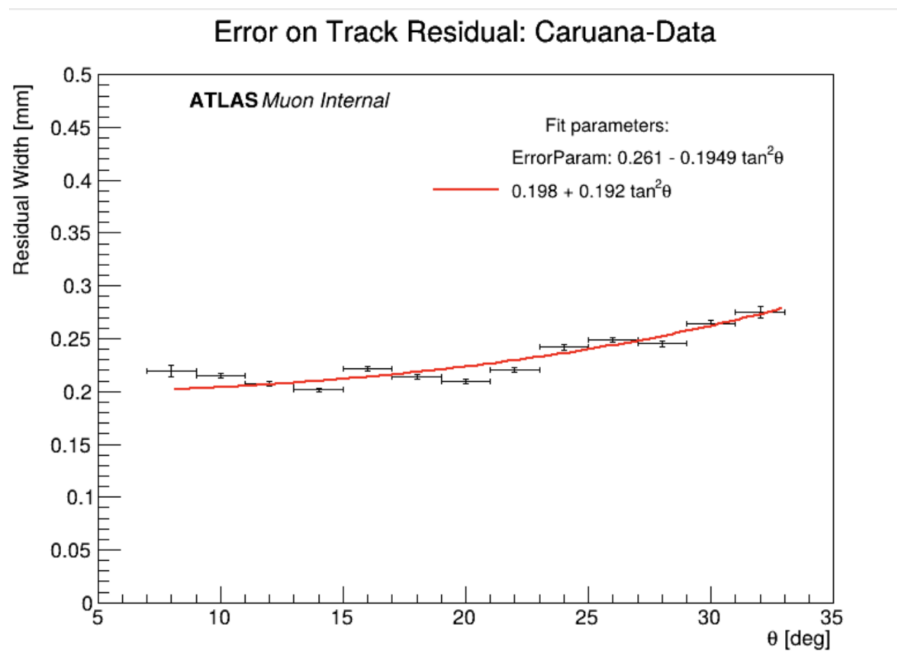
Figure 22: Sample plots of binned angle entries over residual for Centroid and Caruana

As such, the width from the Gaussian fit was extracted and plotted with the entire angle range. This was done to obtain the strip resolution using both methods. Furthermore, the final resolution plot, the comparison was also done for simulated and real data.

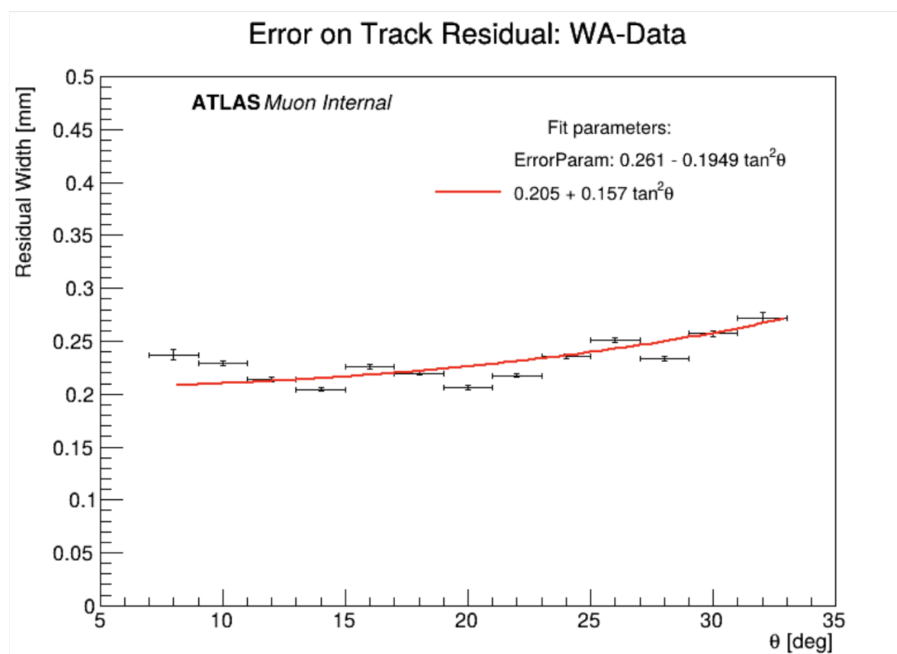
## 6 Results

The following section presents the results obtained from both simulated and real collision data analyses. These results focus on evaluating the spatial resolution, using both the

Centroid and Caruana algorithms as reconstruction methods.



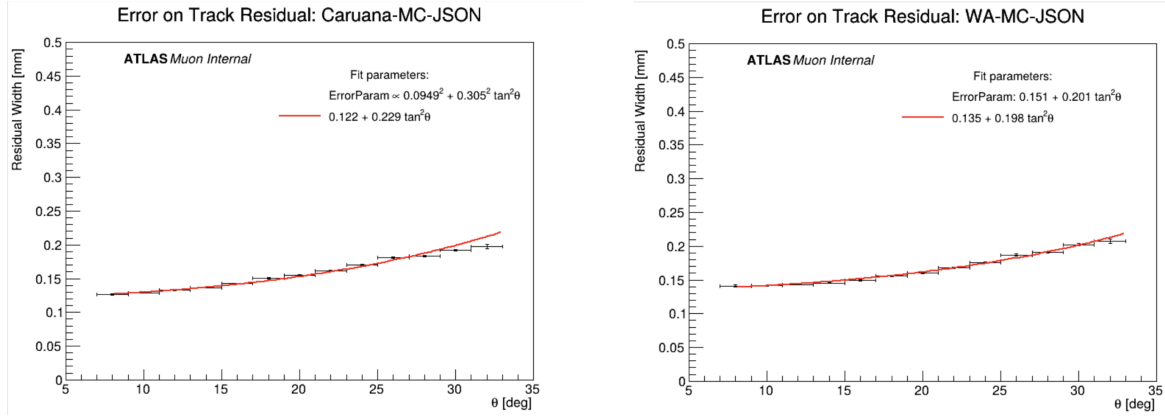
(a) Resolution fitted with Caruana



(b) Resolution fitted with Centroid

Figure 23: Comparison of residual width as a function of muon angle using Caruana (a) and Centroid (b) methods on real ATLAS data

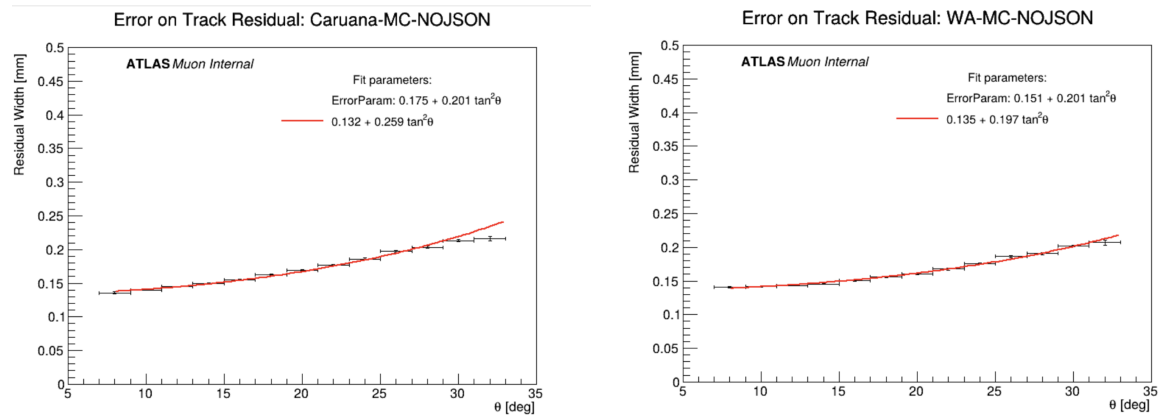
Comparison of residual width as a function of incident muon angle  $\theta$  using (a) Caruana and (b) Centroid (Weighted Average) methods on simulated Monte Carlo data. The Caruana method exhibits a slightly lower baseline resolution and a steeper angular dependence, suggesting improved accuracy in error modeling across incident angles.



(a) Residual width fitted using the Caruana method on Monte Carlo data

(b) Residual width fitted using the Centroid method on Monte Carlo data

Comparison of error parameter fits applied to track residuals from simulated Monte Carlo data



(c) Track Residual Width vs Muon Angle — Caruana (MC-NoJSON)

(d) Track Residual Width vs Muon Angle — Centroid (MC-NoJSON)

Track Residual Width vs Muon Angle from Monte Carlo Simulation Using Caruana and Centroid Methods Top: With JSON ; bottom: Without JSON.

Figure 24: Track residual width as a function of muon angle from Monte Carlo simulations using both Caruana and Centroid methods. Top row: results using error parameters encoded in JSON; bottom row: results without JSON. Subfigures (a) and (c) show fits using the Caruana method, while (b) and (d) show fits using the Centroid method.

These plots demonstrate that the Caruana method consistently provides a tighter fit and better models the angular dependence of the residual width compared to the Centroid method. This trend holds for both JSON-based and non-JSON configurations of the Monte Carlo simulation. The smaller fitted intercepts and more stable angular coefficients in the Caruana results indicate a more accurate and robust error parameterization, especially at low incident angles. The fit values are summarized in Table 3.

Table 3: Error parameter values extracted from resolution fits using the Caruana and Centroid methods across all data types

Fit	$\sigma_0$ [ $\mu\text{m}$ ]	$\mu_0$ [ $\mu\text{m}$ ]
Caruana – MC with JSON	122	229
Centroid – MC with JSON	135	198
Caruana – MC without JSON	132	259
Centroid – MC without JSON	135	197
Caruana – Data	198	192
Centroid – Data	205	157

## 7 Conclusion

This project successfully characterized the spatial resolution of the sTGC strip measurements and evaluated the effectiveness of the Caruana and centroid reconstruction methods as error estimators. From both real and simulated ATLAS data, the Caruana method consistently produced superior results—delivering lower residual widths and more accurate resolution parametrization. These outcomes indicate a more reliable modelling of uncertainty and reduced systematic bias. As a result, muon reconstruction in high-precision tracking was found to be more accurately estimated using the Caruana-based error model. Consequently, it is applicable for integration into future pattern recognition algorithms, with the potential to improve the intrinsic spatial resolution by approximately  $5\mu\text{m}$ .

This work contributes meaningfully to the broader effort of enhancing muon tracking fidelity in the high-luminosity environment of the LHC. Improved resolution yields several tangible benefits for the ATLAS detector during the HL-LHC era: notably, enhanced muon momentum resolution (with 10% precision at 1 TeV) and angular measurements with 1mrad accuracy at the trigger level. Additionally, in synergy with ongoing upgrades to ATLAS subsystems, these improvements are expected to bolster trigger capabilities in high-background conditions and increase pileup rejection by enabling finer separation of overlapping events. Together, these developments will help maintain ATLAS’ precision, scalability, and discovery potential in the years ahead [4, 23].

While this study focused on residual width and spatial resolution as performance benchmarks, it also highlights the need for continued evaluation of uncertainty models under various operating conditions. Future work could explore the robustness of Caruana-based parametrization across broader datasets, including more complex detector configurations or pileup-dominated environments. Ultimately, this project lays the groundwork for improved reconstruction strategies, helping ATLAS remain at the forefront of precision muon tracking throughout the HL-LHC program.

## References

- [1] O. Zomba and A. M. Calibration, “The new small wheel trigger for atlas experiment,” *Nuclear Instruments and Methods in Physics Research Section A: Accelerators, Spectrometers, Detectors and Associated Equipment*, vol. 1067, pp. 169–660, 2024. [Online]. Available: [10.1016/j.nima.2024.169660](https://doi.org/10.1016/j.nima.2024.169660)
- [2] B. Stelzer and A. M. Calibration, “The new small wheel upgrade project of atlas experiment,” *Nuclear and Particle Physics Proceedings*, vol. 273-275, pp. 1160–1164, 2016. [Online]. Available: [10.1016/j.nuclphysbps.2015.09.182](https://doi.org/10.1016/j.nuclphysbps.2015.09.182)
- [3] A. Canesse and A. M. Calibration, “Small-strip thin gap chambers for the muon spectrometer upgrade of the atlas experiment,” in *The Eighth Annual Conference on Large Hadron Collider Physics (LHCP2020)*, vol. 382, 2021. [Online]. Available: [10.22323/1.382.0245](https://doi.org/10.22323/1.382.0245)
- [4] L. Martinelli and A. M. S. group, “Atlas new small wheel performance studies after first year of operation,” *Nuclear Instruments and Methods in Physics Research Section A: Accelerators, Spectrometers, Detectors and Associated Equipment*, vol. 1067, p. 169260, 2024. [Online]. Available: [10.1016/j.nima.2024.169290](https://doi.org/10.1016/j.nima.2024.169290)
- [5] A. Abusleme, C. Bélanger-Champagne, A. Bellerive, Y. Benhammou, J. Botte, H. Cohen, M. Davies, Y. Du, L. Gauthier, T. Koffas, S. Kuleshov, B. Lefebvre, C. Li, N. Lupu, G. Mikenberg, D. Mori, J. Ochoa-Ricoux, E. Perez Codina, S. Rettie, A. Robichaud-Véronneau, and C. Zhu, “Performance of a full-size small-strip thin gap chamber prototype for the atlas new small wheel muon upgrade,” *Nuclear Instruments and Methods in Physics Research Section A: Accelerators, Spectrometers, Detectors and Associated Equipment*, vol. 817, pp. 85–92, 2016. [Online]. Available: [10.1016/j.nima.2016.01.087](https://doi.org/10.1016/j.nima.2016.01.087)
- [6] T. Kawamoto, S. Vlachos, L. Pontecorvo, J. Dubbert, G. Mikenberg, P. Iengo, C. Dallapiccola, C. Amelung, L. Levinson, and R. Richter, “New small wheel technical design report (cern-lhcc-2013-006; atlas-tdr-020),” CERN. The LHC Experiments Committee, Tech. Rep., 2013. [Online]. Available: <http://cdsweb.cern.ch/record/1552862/>
- [7] J. Chapman, T. Dai, E. Diehl, H. Feng, L. Guan, J. Yu, J. Wang, B. Zhou, and J. Zhu, “Simulation studies for stgc,” University of Michigan, Tech. Rep., n.d. [Online]. Available: <https://indico.cern.ch/event/245152/contributions/1565612/attachments/419829/582993/TGCsim.BNL.pdf>
- [8] A. M. C. Sekhniaidze, G., “Construction and performance of the stgc and micromegas chambers for atlas nsw upgrade,” in *14th Topical Seminar on Innovative Particle and Radiation Detectors*, 2016. [Online]. Available: [10.1088/1748-0221/12/03/C03020](https://doi.org/10.1088/1748-0221/12/03/C03020)
- [9] ATLAS Collaboration, “Collision events seen by atlas,” [https://opendata.atlas.cern/docs/atlas/atlas\\_events](https://opendata.atlas.cern/docs/atlas/atlas_events), n.d., accessed: 20 April 2025.
- [10] B. Lefebvre, “Characterization studies of small-strip thin gap chambers for the atlas upgrade,” Ph.D. dissertation, Carleton University, 2018. [Online]. Available: <https://cds.cern.ch/record/2633639/files/CERN-THESIS-2018-111.pdf>

- [11] K. Kleinknecht, *Detectors for Particle Radiation*. Cambridge, UK: Cambridge University Press, 1987.
- [12] C. Kitsaki and A. M. Collaboration, “The atlas new small wheel simulation and reconstruction software and detector performance studies,” in *40th International Conference on High Energy physics - ICHEP2020*, 2020. [Online]. Available: <https://cds.cern.ch/record/2746465/files/ATL-MUON-PROC-2020-022.pdf>
- [13] T. A. Collaboration, “Performance of the atlas rpc detector and level-1 muon barrel trigger at  $s = 13$  tev,” *Journal of Instrumentation*, 2021. [Online]. Available: 10.1088/1748-0221/16/07/P07029
- [14] A. Collaboration, “Atl-muon-slide-2022-206,” ATLAS Collaboration, Tech. Rep., 2022. [Online]. Available: <https://cds.cern.ch/record/2811136/files/ATL-MUON-SLIDE-2022-206.pdf>
- [15] L. Burke, “stgc athena digitization reconstruction tuning guide,” 2024.
- [16] W. R. Leo, *Techniques for Nuclear and Particle Physics Experiments: A How-To Approach*. Berlin: Springer Berlin / Heidelberg, 1994, ch. 4.4.5, accessed via ProQuest Ebook Central. [Online]. Available: <https://ebookcentral-proquest-com.proxy.library.carleton.ca/lib/oculcarleton-ebooks/detail.action?docID=3089885>
- [17] H. Guo, “A simple algorithm for fitting a gaussian function,” *IEEE Signal Processing Magazine*, vol. 28, pp. 134–137, 09 2011. [Online]. Available: 10.1002/9781118316948.ch31
- [18] E. Pastuchová, “Comparison of algorithms for fitting a gaussian function used in testing smart sensors,” *Journal of Electrical Engineering*, vol. 66, 2015, elena.pastuchova@stuba.sk. [Online]. Available: 10.2478/jee-2015-0029
- [19] M. Sloan, “stgc single point resolution analysis for atlas’ new small wheel,” Carleton University, Tech. Rep., 2020. [Online]. Available: [https://particlephysics.ca/wp/wp-content/uploads/CERN\\_summer\\_student\\_report\\_2020\\_Michael\\_Sloan.pdf](https://particlephysics.ca/wp/wp-content/uploads/CERN_summer_student_report_2020_Michael_Sloan.pdf)
- [20] L. Demortier and L. Lyons, “Everything you always wanted to know about pulls,” CDF/ANAL/PUBLIC/5776, Tech. Rep., 2002. [Online]. Available: [https://hep-physics.rockefeller.edu/luc/technical\\_reports/cdf5776-pulls.pdf](https://hep-physics.rockefeller.edu/luc/technical_reports/cdf5776-pulls.pdf)
- [21] R. Kissell and J. Poserina, “Chapter 4 - advanced math and statistics,” in *Optimal Sports Math, Statistics and Fantasy*, 2017, pp. 103–135. [Online]. Available: 10.1016/B978-0-12-805163-4.00004-9
- [22] H. Johnson, R. Van Beers, and P. Haggard, “Action and awareness in pointing tasks,” *Experimental Brain Research*, vol. 146, no. 4, pp. 451–459, 2002. [Online]. Available: 10.1007/s00221-002-1200-z
- [23] G. Aad, B. Abbott, D. Abbott, J. Abdallah, K. Abeling, S. Abidi, A. Aboulhorma, S. Abovyan, H. Abramowicz, H. Abreu, and A. Collaboration, “The ATLAS experiment at the CERN Large Hadron Collider: a description of the detector configuration for Run 3,” *Journal of Instrumentation*, vol. 19, no. 05, p. P05063, 2024.